In preparation for *ApJ*. March 1, 2013 2:28.
Preprint typeset using LaTeX style emulateapj v. 8/13/10

arXiv:1302.7003v1 [astro-ph.EP] 27 Feb 2013

SPITZER OBSERVATIONS OF THE THERMAL EMISSION FROM WASP-43B

Jasmina Blecic[1], Joseph Harrington[1, 2], Nikku Madhusudhan[3], Kevin B. Stevenson[1], Ryan A. Hardy[1], Patricio E. Cubillos[1, 2], Matthew Hardin[1], Sarah Nymeyer[1], David R. Anderson[4], Coel Hellier[4], Alexis M. S. Smith[4] and Andrew Collier Cameron[5]

[1] Planetary Sciences Group, Department of Physics, University of Central Florida, Orlando, FL 32816-2385, USA
[2] Max-Planck-Institut für Astronomie, D-69117 Heidelberg, Germany
[3] Department of Physics and Department of Astronomy, Yale University, New Haven, CT 06511, USA
[4] Astrophysics Group, Keele University, Keele, Staffordshire ST5 5BG, UK and
[5] SUPA, School of Physics and Astronomy, University of St. Andrews, North Haugh, St. Andrews, Fife KY16 9SS, UK

In preparation for ApJ. *March 1, 2013 2:28.*

ABSTRACT

WASP-43b (Hellier et al.; Gillon et al.) is one of the closest-orbiting hot Jupiters, with a semimajor axis $a = 0.01526 \pm 0.00018$ AU and a period of only 0.81 days. However, it orbits one of the coolest stars with a hot Jupiter (K7V, $T_* = 4520 \pm 120$ K), giving the planet a modest equilibrium temperature of $T_{\rm eq} = 1440 \pm 40$ K, assuming zero Bond albedo and uniform planetary energy redistribution. This has resulted in strong signal-to-noise-ratio (S/N) observations and deep eclipses in both *Warm Spitzer* channels (3.6 and 4.5 μm). Planets with higher S/N allow more accurate measurements of eclipse depths and brightness temperatures, placing tighter constraints on atmospheric composition and thermal structure. The eclipse depths and brightness temperatures from our jointly fit model are $0.346 \pm 0.013\%$ and 1684 ± 24 K at 3.6 μm and $0.382 \pm 0.015\%$ and 1485 ± 24 K at 4.5 μm. The eclipse timings improved the estimate of the orbital period, P, by a factor of three ($P = 0.81347459 \pm 2.1\times10^{-7}$ days) compared to Gillon et al. and put an upper limit on the eccentricity ($e = 0.007^{+0.013}_{-0.004}$). We use our *Spitzer* eclipse depths with two previously reported ground-based data points in the J and K bands to constrain the atmospheric properties of WASP-43b. The data rule out a strong thermal inversion in the dayside atmosphere of WASP-43b. Model atmospheres with no thermal inversions and fiducial oxygen-rich compositions are able to explain all the available data. These data, however, are insufficient to place stringent constraints on the molecular mixing ratios. The data suggest low day-night energy redistribution in the planet, consistent with previous studies, with a nominal upper limit of about 35% for the fraction of energy incident on the dayside, but redistributed to the nightside.

Subject headings: Extrasolar Planets — eclipses — planets and satellites: atmospheres — planets and satellites: individual (WASP-43b) — techniques: photometric

1. INTRODUCTION

Recent *Kepler* results (Borucki et al. 2011; Batalha et al. 2012) have shown a striking increase in detections of the smallest candidates, and the planet-candidate lists now show that hot Jupiters are much less common than planets smaller than Neptune. But, nearly all *Kepler* candidates are too small, cold, or distant for atmospheric characterization, except the nearby hot Jupiters. Their host stars, bright enough for radial velocity (RV) measurements, subject these planets to a strong irradiating flux, which governs their atmospheric chemistry and dynamics. Their large sizes and large scale heights (e.g., Showman & Guillot 2002) give the signal-to-noise ratio (S/N) needed for basic atmospheric characterization.

The most common technique for observing hot Jupiters and characterizing their dayside atmospheres is secondary eclipse photometry (e.g., Fraine et al. 2013; Crossfield et al. 2012; Todorov et al. 2012; Desert et al. 2012; Deming et al. 2011; Beerer et al. 2011; Demory et al. 2007). During secondary eclipse, when the planet passes behind its star, we see a dip in integrated flux proportional to the planet-to-star flux ratio, or usually 0.02–0.5% in the *Spitzer Space Telescope* infrared wavelengths, where the signal is strongest. This dip is much lower at wavelengths accessible from the ground or from the *Hubble Space Telescope*. Techniques such as phase-curve measurement (Knutson et al. 2009, 2012; Lewis et al. 2013; Cowan et al. 2012a,b; Crossfield et al. 2010), eclipse spectroscopy (Deming et al. 2013; Gibson et al. 2012; Berta et al. 2012), and ingress-egress mapping (de Wit et al. 2012; Majeau et al. 2012) can reveal more than a secondary eclipse, but are available for only a small number of high-S/N planets.

A secondary eclipse observed at one wavelength constrains an exoplanet's temperature. Multiple wavelengths constrain the planet's dayside spectrum, potentially yielding insight into the atmospheric composition and temperature structure. Different wavelengths probe different atmospheric levels and can be combined into a broadband spectrum for further atmospheric modeling (e.g., Madhusudhan & Seager 2009; Stevenson et al. 2010). Infrared observations are specifically valuable because the most abundant chemical species in planetary atmospheres (aside from H_2 and He), such as H_2O, CO, CO_2, and CH_4, have significant absorption and emission features at these wavelengths (e.g., Madhusudhan & Seager 2010). Constraints on chemical composition and thermal structure are important for both further atmospheric modeling (e.g., Showman et al. 2009) and studies of the planet's formation.

Secondary eclipse observations also provide insight into the exoplanet's orbit. Measuring the time of the secondary eclipse relative to the time of transit can establish an upper limit on orbital eccentricity, e, and constrain the argument of periapsis,

jasmina@physics.ucf.edu

ω, independently of RV measurements. Orbital eccentricity is important in dynamical studies and in calculating irradiation levels. Apsidal precession can also be constrained by eclipse timing and can be used to reveal the degree of central concentration of mass in the planetary interior (Ragozzine & Wolf 2009; Campo et al. 2011; López-Morales et al. 2010).

WASP-43b was first detected by the Wide-Angle Search for Planets (WASP) team (Hellier et al. 2011) in 2009 and 2010 from the WASP-South and WASP-North observatories. The WASP team also performed follow-up measurements with the CORALIE spectrograph, the TRAPPIST telescope, and EulerCAM in December 2010. These observations revealed a planet with a mass M_p = 1.78 Jupiter masses (M_J) and a radius R_p = 0.93 Jupiter radii (R_J), transiting one of the coldest stars to host a hot Jupiter (type K7V, $T_* = 4400 \pm 200$ K). They found the planet to have an exceptionally short orbital period of 0.81 days and a semi-major axis of only 0.0142 AU, assuming the host star has a mass of $M_* = 0.58 \pm 0.05\ M_\odot$. The planet's orbital eccentricity was constrained to $e < 0.04$ at 3σ. Spectroscopic measurements of the star revealed a surface gravity of $\log(g) = 4.5 \pm 0.2$ (cgs) and a projected stellar rotation velocity of $v_* \sin(i) = 4.0 \pm 0.4$ km s^{-1}, where i is the inclination of the star's pole to the line of sight. Strong Ca H and K emission indicates that the star is active.

Gillon et al. (2012) presented an extensive analysis of twenty-three transit light curves, seven occultations, and eight new measurements of the star's RV, observed during 2010 and 2011 with TRAPPIST, the Very Large Telescope (VLT), and EulerCAM. They improved the parameters of the system significantly ($e = 0.0035 \pm 0.0043$, $M_\mathrm{p} = 2.034 \pm 0.052\ M_\mathrm{J}$, $R_\mathrm{p} = 1.036 \pm 0.019\ R_\mathrm{J}$), refined stellar parameters ($T_\mathrm{eff} = 4520 \pm 120$ K, $M_* = 0.717 \pm 0.025\ M_\odot$, $R_* = 0.667 \pm 0.011\ R_\odot$), and constrained stellar density ($\rho_* = 2.41 \pm 0.08\ \rho_\odot$). They also confirmed that the observed variability of the transit parameters can be attributed to the variability of the star itself (consistent with Hellier et al. 2011). In addition, they detected the planet's thermal emission at 1.19 μm and 2.09 μm, inferring poor redistribution of heat to the night side and an atmosphere without a thermal inversion, using the atmospheric models of Fortney et al. (2005, 2008).

In this paper we present two secondary eclipses, observed with the *Spitzer Space Telescope* at 3.6 and 4.5 μm using the Infrared Array Camera (IRAC; Fazio et al. 2004), which further constrain the dayside emission of the planet and improve the orbital parameters of the system. We combine our eclipse-depth measurements with those of Gillon et al. (2012) to constrain the planetary atmosphere model, energy redistribution, and presence of thermal inversion using the Madhusudhan & Seager retrieval method.

The following sections present our observations; discuss photometric analysis; explain specific steps taken to arrive at the fits for each observation and a joint fit; give improved constraints on the orbital parameters based on available RV, eclipse, and transit data; discuss implications for the planetary emission spectrum and planetary composition; state our conclusions; and, in the Appendix, supply the full set of system parameters from our own and previous work. The electronic attachment to this paper includes archival light curve files in FITS ASCII table and IRSA formats.

2. OBSERVATIONS

We observed two secondary eclipses of WASP-43b with the *Spitzer* IRAC camera in subarray mode (Program ID 70084). A sufficiently long baseline (Figure 1) was monitored before the eclipses, providing good sampling of all *Spitzer* systematics. To minimize intrapixel variability each target had fixed pointing. We used the Basic Calibrated Data (BCD) from *Spitzer*'s data pipeline, version S.18.18.0. Basic observational information is given in Table 1.

TABLE 1
OBSERVATION INFORMATION

Channel	Observation Date	Start Time [MJD$_\mathrm{UTC}$]	Duration [s]	Exposure Time [s]	Number of Frames
Ch1	2011-07-30	2455772.6845	21421	2	10496
Ch2	2011-07-29	2455771.8505	21421	2	10496

3. SECONDARY-ECLIPSE ANALYSIS – METHODOLOGY

Exoplanet characterization requires high precision, since the planets' inherently weak signals are weaker than the systematics. In addition, *Spitzer*'s systematics lack full physical characterizations. We have developed a modular pipeline, Photometry for Orbits, Eclipses, and Transits (POET), that implements a wide variety of treatments of systematics and uses Bayesian methods to explore the parameter space and information criteria for model choice. The POET pipeline is documented in our previous papers (Stevenson et al. 2010; Campo et al. 2011; Nymeyer et al. 2011; Stevenson et al. 2012; Blecic et al. 2013; Cubillos et al. 2013), so we give here just a brief overview of the specific procedures used in this analysis.

The pipeline uses *Spitzer*-supplied BCD frames to produce systematics-corrected light curves and parameter and uncertainty estimates, routinely achieving 85% of the photon noise limit or better. Initially, POET masks pixels according to *Spitzer's* permanent bad pixel masks, and then it additionally flags bad pixels (energetic particle hits, etc.) by grouping sets of 64 frames and performing a two-iteration, 4σ rejection at each pixel location. Image centers with 0.01 pixel accuracy come from testing a variety of centering routines (Stevenson et al. 2010, Supplementary Information). Subpixel 5× interpolated aperture photometry (Harrington et al. 2007) produces the light curves. We omit frames with bad pixels in the photometry aperture. The background, subtracted before photometry, is an average of good pixels within an annulus centered on the star in each frame.

Detector systematics vary by channel and can have both temporal (detector ramp) and spatial (intrapixel variability) components. At 3.6 and 4.5 μm, intrapixel sensitivity variation is the dominant effect (Charbonneau et al. 2005), so accurate centering at the 0.01 pixel level is critical. We fit this systematic with a Bilinearly-Interpolated Subpixel Sensitivity (BLISS) mapping technique, following Stevenson et al. (2012), including the method to optimize the bin sizes and the minimum number of data points per bin.

At 5.8, 8.0, and 16 μm, there is temporal variability, attributed to charge trapping (Knutson et al. 2009). Weak temporal dependencies can also occur at 3.6 and 4.5 μm (Reach et al. 2005; Charbonneau et al. 2005; Campo et al. 2011; Blecic et al. 2013), while weak spatial variability has been seen at 5.4 and 8.0 μm (Stevenson et al. 2012; Anderson et al. 2011). Thus, we consider both systematics in all channels when determining the best-fit model.

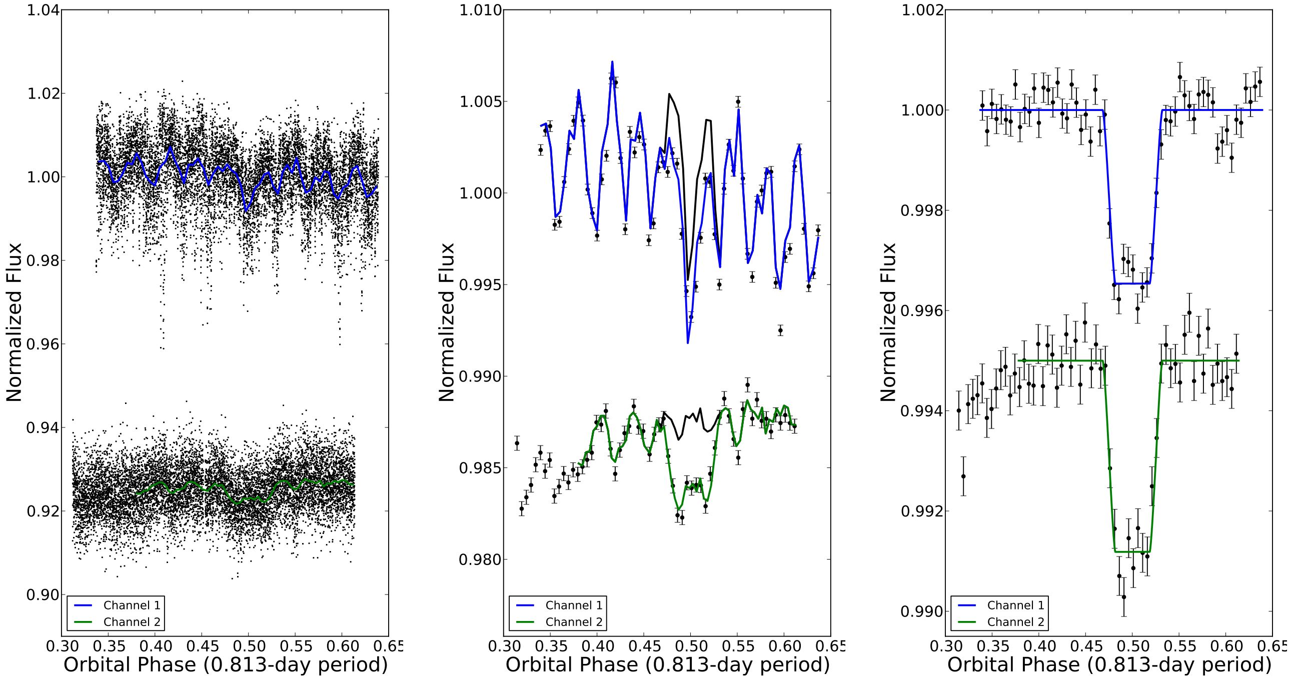

FIG. 1.— Raw (left), binned (center, 60 points per bin, with 1σ error bars), and systematics-corrected (right) secondary-eclipse light curves of WASP-43b at 3.6 and 4.5 µm. The results are normalized to the system flux and shifted vertically for comparison. Note the different vertical scales used in each panel. The colored lines are best-fit models. The black curves in panel 2 are models without eclipses. As seen in the binned plots of channel 2, a ramp model is not needed to correct for the time-dependent systematic if initial data points affected by pointing drift are clipped (see Section 3).

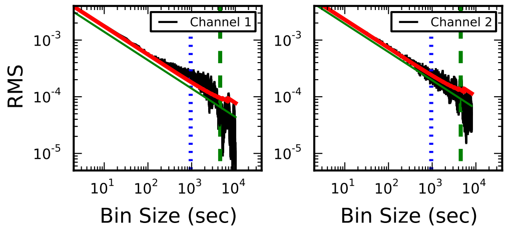

FIG. 2.— Correlations of the residuals for the two secondary eclipses of WASP-43b, following Pont et al. (2006). The black line represents the RMS residual flux *vs.* bin size. The red line shows the predicted standard error scaling for Gaussian noise. The green line shows the Poisson noise. The black vertical lines at each bin size depict 1σ uncertainties on the RMS residuals ($RMS/\sqrt{2N}$, where N is the number of bins). The dotted vertical blue line indicates the ingress/egress timescale, and the dashed vertical green line indicates the eclipse duration timescale. Large excesses of several σ above the red line would indicate correlated noise at that bin size. Inclusion of 1σ uncertainties shows no noise correlation on the timescale between the ingress/egress and the eclipse-duration time.

We fit the model components simultaneously using a Mandel & Agol (2002) eclipse, $E(t)$; the time-dependent detector ramp model, $R(t)$; and the BLISS map, $M(x,y)$:

$$F(x,y,t) = F_s R(t) M(x,y) E(t), \tag{1}$$

where $F(x,y,t)$ is the aperture photometry flux and F_s is the constant system flux outside of the eclipse.

To choose the best systematics models and aperture size, we analyze dozens of model combinations and use goodness-of-fit criteria (Campo et al. 2011). To choose the best aperture size and the number of initial points dropped during instrument settling for a given channel, we minimize the standard deviation of the normalized residuals (SDNR). Ignoring data points from the beginning of the observation is a common procedure (Knutson et al. 2011) when searching for the best-fitting ramp. We remove the smallest number of points consistent with the minimal SDNR.

Once we have found the best dataset in this way, we compare different ramp models by applying either the Akaike Information Criterion:

$$\mathrm{AIC} = \chi^2 + 2k, \tag{2}$$

where k is the number of free parameters, or the Bayesian Information Criterion:

$$\mathrm{BIC} = \chi^2 + k \ln N, \tag{3}$$

where N is the number of data points. The best model minimizes the chosen criterion. For the final decision, the level of correlation in the photometric residuals is also considered, by plotting root-mean-squared (RMS) model residuals *vs.* bin size (time interval; Pont et al. 2006; Winn et al. 2008; Campo et al. 2011) and comparing this to the theoretical $1/\sqrt{N}$ RMS scaling.

We explore the phase space and estimate errors using a Markov-chain Monte Carlo (MCMC) routine following the Metropolis-Hastings random-walk algorithm, which uses independent Gaussian proposal distributions for each parameter with widths chosen to give an acceptance rate of 30-60%. Each MCMC model fit begins with the Levenberg-Marquardt algorithm (least-squares minimization). We use a Bayesian prior (e.g., Gelman 2002) if a parameter's uncertainty in the literature is smaller than what we can achieve. We then run enough MCMC iterations to satisfy the Gelman & Rubin (1992) convergence test. After every run, we assess convergence by examining plots of the parameter traces, pairwise correlations, autocorrelations, marginal posteriors, best-fitting model, and systematics-corrected best-fitting model. The final fit is obtained from the simultaneous run of all datasets, sharing parameters such as the eclipse midpoint and duration among some or all datasets.

We report the times of our secondary eclipses in both $\mathrm{BJD_{UTC}}$ (Coordinated Universal Time) and $\mathrm{BJD_{TT}}$ ($\mathrm{BJD_{TDB}}$, Barycentric Dynamical Time), calculated using the Jet Propulsion Laboratory (JPL) Horizons system and following Eastman et al. (2010).

4. SECONDARY-ECLIPSE ANALYSIS – FIT DETAILS

Light curves for both channels were extracted using every aperture radius from 2.00 to 4.50 pixels, in 0.25 pixel increments. A 2D Gaussian fit found stellar centroids most consistently. We estimated the background flux using an annulus of 7–15 pixels from the center of the star for both channels. For the secondary-eclipse ingress and egress time, we used a Bayesian prior (t_{2-1} = 950.5 ± 145.5 s), calculated from unpublished WASP photometric and RV data.

Figure 1 shows our systematics-corrected, best-fit light curve models. Figure 2 presents the scaling of the RMS model residuals *vs.* bin size for both channels, which shows no significant time correlation in the residuals.

4.1. *Channel 1 – 3.6 μm*

The most prominent systematic in this *Spitzer* channel is the intrapixel effect. The best BLISS-map bin size is 0.006 pixels when we exclude bins with less than 4 measurements. The ramp and eclipse models fit without removing initial data points. The smallest value of BIC reveals that the best ramp model is quadratic; this model is 1.2×10^{30} times more probable then the next best (linear) model. Table 2 lists the best ramp models, comparing their SDNR, BIC values, and eclipse depths.

TABLE 2
CHANNEL 1 RAMP MODELS

Ramp Model	SDNR	ΔBIC	Eclipse Depth [%]
Quadratic	0.0039001	0.0	0.344 ± 0.013
Rising	0.0039113	56.8	0.292 ± 0.012
No-Ramp	0.0039315	144.4	0.268 ± 0.012
Linear	0.0039293	142.1	0.270 ± 0.012

Figure 3 shows a comparison between the best ramp models and their SDNR and BIC values through all aperture sizes, indicating which aperture size is the best and which model has the lowest BIC value.

Photometry generates consistent eclipse depths for all tested apertures, with the lowest SDNR at an aperture radius of 2.50 pixels (Figure 4).

4.2. *Channel 2 – 4.5 μm*

In this channel, we noticed an upward trend in flux at the beginning of the observation, possibly due to telescope settling, which we do not model. We clipped 2300 initial data points (∼38 minutes of observation), the smallest number of points consistent with the minimal SDNR. The 2.50 pixel aperture radius minimizes SDNR (Figure 5).

To remove intrapixel variability, the BLISS bin size is 0.016 pixels, ignoring bins with less than 4 points. The ramp models indicate a negligible ramp variation. The lowest BIC value corresponds to the model without a ramp (Table 3). The no-ramp model is 78 times more probable than the linear model.

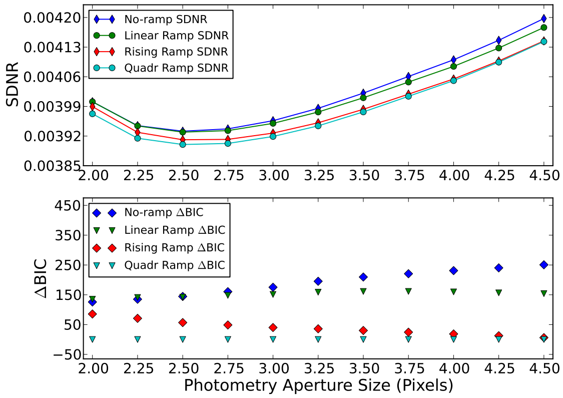

FIG. 3.— Channel 1 comparison between different ramp models. The plots show SDNR *vs.* aperture size and ΔBIC *vs.* aperture size. A lower SDNR value indicates a better model fit. The lowest SDNR value marks the best aperture size (2.50 pixels). A lower ΔBIC value at the best aperture size indicates which ramp model is the best (quadratic ramp model, green triangles).

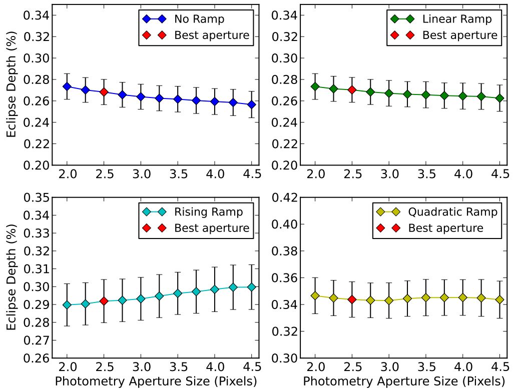

FIG. 4.— The best-fit eclipse depths as a function of photometry aperture size for channel 1. The best four ramp models are plotted. The red point indicates the best aperture size for that channel. The eclipse-depth uncertainties are the result of 10^5 MCMC iterations. The trend shows insignificant dependence of eclipse depth on aperture size (much less than 1σ).

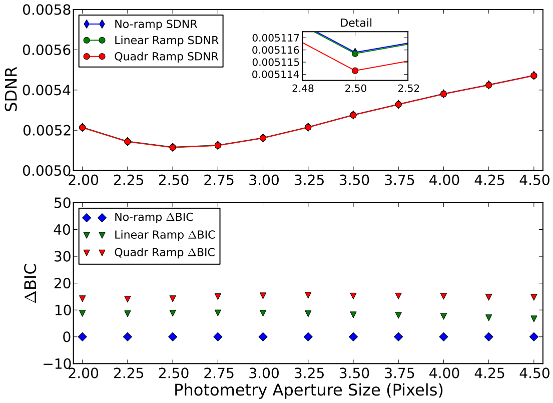

FIG. 5.— Channel 2 comparison between different ramp models. Plot shows SDNR *vs.* aperture size and ΔBIC *vs.* aperture size. A lower SDNR value indicates a better model fit. The lowest SDNR value marks the best aperture size (2.50 pixels). Lower BIC values at the best aperture size indicate better models (best: no-ramp model, blue diamonds). The inset shows separation in SDNR for different ramp models at the best aperture size.

We tested the dependence of eclipse depth on aperture ra-

TABLE 3
CHANNEL 2 RAMP MODELS

Ramp Model	SDNR	ΔBIC	Eclipse Depth [%]
No-Ramp	0.0051158	0	0.392 ± 0.016
Linear	0.0051157	8.8	0.392 ± 0.016
Quadratic	0.0051143	14.2	0.409 ± 0.019

dius, showing that they are all well within 1σ of each other, to validate the consistency of our models (Figure 6).

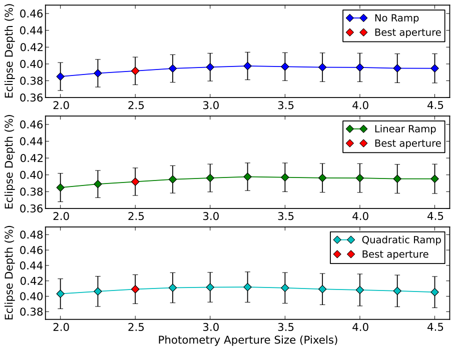

FIG. 6.— The best-fit eclipse depths as a function of photometry aperture size for channel 2. The three best ramp models are plotted. The red point indicates the best aperture size for that channel. The eclipse-depth uncertainties are the result of 10^5 MCMC iterations. The trend shows negligible dependence of eclipse depth on aperture size (much less than 1σ).

4.3. *Joint Fit*

To improve S/N on the eclipse depths, we share the eclipse width (duration) and eclipse midpoint phases in a joint fit of both datasets. The best ramp models and the best aperture sizes from the separate channel analyses are used in the joint fit. To produce the best joint-model fits, we iterated MCMC until the Gelman & Rubin (1992) diagnostics for all parameters dropped below 1%, which happened after 10^5 iterations.

The best joint-model fit parameters are in Table 4. Files containing the light curves, best model fits, centering data, photometry, etc., are included as electronic supplements to this article. The eclipse-midpoint time is further used for the subsequent orbital analysis, and the eclipse depths are used for the atmospheric analysis.

5. ORBIT

The eclipse midpoint (after a 15.2 second correction for the eclipse-transit light-time) has a phase of 0.5001 ± 0.0004, so $e\cos\omega = 0.0001 \pm 0.0006$, or a 3$\sigma$ upper limit of $|e\cos\omega| < 0.0018$, consistent with a circular orbit.

To improve the orbit solution further, we combined data from our observations with data from a variety of sources. Transit midpoint times were taken from Hellier et al. (2011) and Gillon et al. (2012), and amateur observations were listed in the Exoplanet Transit Database (see Table 5). We used *CORALIE* RV observations published by Hellier et al. (2011) and Gillon et al. (2012). No RV points needed removal due to the Rossiter-McLaughlin effect. We subtracted 15.2 seconds from the eclipse midpoints to correct for light-travel time across the orbit. We corrected all points to TDB, if this was not already done (Eastman et al. 2010). We converted the amateur data from HJD to BJD, putting all times in a consistent $\mathrm{BJD_{TDB}}$ format. There were 49 transit points, 23 RV points, and one effective eclipse observation. We fit all of these data simultaneously, as described by Campo et al. (2011). The free parameters in this fit were $e\sin\omega$; $e\cos\omega$; P; the reference transit midpoint time, T_0; the RV semi-amplitude, K; and the RV offset, γ. The addition of the amateur transit observations improves the uncertainty of P by a factor of three compared to Gillon et al. (2012), reducing it to 18 milliseconds. The fit finds an eccentricity of $0.007^{+0.013}_{-0.004}$, consistent with a circular orbit and expectations for a close-in planet, where eccentricity should be damped by tidal interactions with the host star. The fit results are summarized in Table 6.

Because the bulk of the eccentricity signal for WASP-43b comes from $e\sin\omega$, and ω is practically unconstrained, it is likely that this eccentricity signal comes from the planet's interaction with the stellar tidal bulge. Arras et al. (2012) predict that the RV semi-amplitude of this effect is 8.9 ms^{-1}. Since our model shows that $eK = 3.9^{+7.1}_{-2.2}$ ms^{-1}, it is possible that the majority or entirety of this signal is due to the tidal bulge interaction, and the true eccentricity is closer to the upper limit deduced from the secondary eclipse.

We found that, for a linear ephemeris fit, there is considerable scatter in O-C (observed time minus calculated time). The root-mean-square of the stated transit-time uncertainties is 27 seconds, while the standard deviation of the residuals is 78 seconds. WASP-43b is close enough to its host star that tidal decay is a significant factor in its evolution, so we attempted to estimate the decay rate by adding a quadratic term to our ephemeris model, following Adams et al. (2010). Our model for the transit ephemeris is now:

$$T_N = T_0 + PN + \delta P \frac{N(N-1)}{2}, \tag{4}$$

where N is the number of orbits elapsed since the epoch T_0, P is the orbital period at T_0, and $\delta P = \dot{P}P$, where $\dot{P}$ is the short-term rate of change in the orbital period. Fitting this model to the transit data, we find that $\delta P = (-1.7 \pm 0.3) \times 10^{-8}$ days orbit^{-2}, or $\dot{P} = -0.65 \pm 0.12$ s year^{-1}. This is illustrated in Figure 7. This would be a 5σ detection, and is about ten times

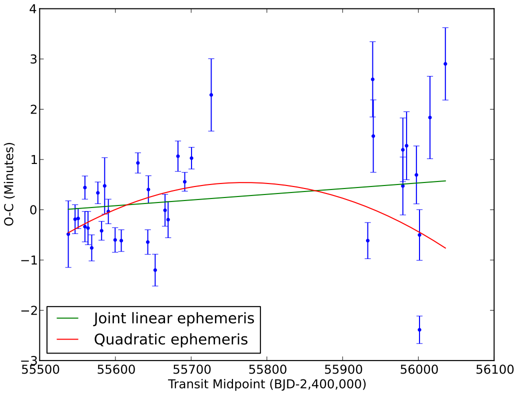

FIG. 7.— O-C diagram for transit observations of WASP-43b with respect to the best linear ephemeris fit to the transits. Only points with an Exoplanet Transit Database quality rating of 3 or higher are shown here and used in this analysis. The red line represents the full quadratic ephemeris and shows that transits are progressively occurring earlier. The green line shows an ephemeris that best fits the RV and eclipse data in addition to the transit data. The quadratic trend depends largely on two outliers with relatively small uncertainties.

TABLE 4
2-JOINT BEST-FIT ECLIPSE LIGHT-CURVE PARAMETERS.

Parameter	Channel 1	Channel 2
Array Position ($\bar{x}$, pix)	14.99	14.8
Array Position ($\bar{y}$, pix)	15.01	15.05
Position Consistency[a] (δ_x, pix)	0.005	0.01
Position Consistency[a] (δ_y, pix)	0.006	0.007
Aperture Size (pix)	2.5	2.5
Sky Annulus Inner Radius (pix)	7.0	7.0
Sky Annulus Outer Radius (pix)	15.0	15.0
System Flux F_s (μJy)	64399.0 ± 5.0	37911.0 ± 2.0
Eclipse Depth (%)	0.346 ± 0.013	0.382 ± 0.015
Brightness Temperature (K)	1684.0 ± 24.0	1485.0 ± 24.0
Eclipse Midpoint (orbits)	0.5002 ± 0.0004	0.5002 ± 0.0004
Eclipse Midpoint (BJD$_{\rm UTC}$ - 2,450,000)	5773.3172 ± 0.0003	5772.5037 ± 0.0003
Eclipse Midpoint (BJD$_{\rm TDB}$ - 2,450,000)	5773.3179 ± 0.0003	5772.5045 ± 0.0003
Eclipse Duration (t_{4-1}, hrs)	1.25 ± 0.02	1.25 ± 0.02
Ingress/Egress Time (t_{2-1}, hrs)	0.264 ± 0.018	0.264 ± 0.018
Ramp Name	quadramp	no-ramp
Ramp, Quadratic Term	3e-05 ± 0.0004	0 ±
Ramp, Linear Term	-0.082716 ± 0.007	0 ±
Intrapixel Method	BLISS	BLISS
BLISS Bin Size in x (pix)	0.006	0.016
BLISS Bin Size in y (pix)	0.006	0.016
Minimum Number of Points per Bin	4	4
Total Frames	10496	10496
Frames Used	10124	8004
Rejected Frames (%)	0.44	1.12
Free Parameters	7	2
Number of Data Points in Fit	10124	8004
AIC Value	18137.0	18137.0
BIC Value	18207.2	18207.2
SDNR	0.0039006	0.0051168
Percentage of Photon-Limited S/N (%)	80.3	85.0

[a] RMS frame-to-frame position difference.

the value of -0.060 ± 0.015 s year^{-1} found by Adams et al. (2010) for OGLE-TR-113b. The BIC values strongly favor the quadratic (decaying) ephemeris (BIC = 242) over the linear ephemeris (BIC = 271). The transit ephemeris models are summarized in Table 7.

As the circularity of WASP-43b's orbit is well established by the RV data and confirmed by the eclipse data for a linear ephemeris, our secondary-eclipse point should not be expected to deviate from an eclipse phase of 0.5 in a quadratic ephemeris. Assuming a circular orbit where eclipses occur at $N + \frac{1}{2}$, the eclipse time should be given by:

$$T_{N+\frac{1}{2}} = T_0 + P\left(N + \frac{1}{2}\right) + \frac{1}{2}\delta P\left(N^2 - \frac{1}{4}\right). \qquad (5)$$

We find that our eclipse time matches this ephemeris within errors, lending further support to the quadratic fit.

However, both fits look poor by eye. The standard deviation of the residuals about the quadratic ephemeris is 66 seconds, still much larger than the 27 second typical transit time uncertainty. The reduced χ^2 for the quadratic fit is $\sim$8, so much of the residual scatter is unexplained by both models. Either an actual variability in transit timing exists, or there were problems in the data processing or reporting. The quadratic trend is largely dependent on two outliers with very small uncertainties. Could there be mistakes in the time corrections for heterogeneous transit data? This is unlikely because the Exoplanet Transit Database indicates that all amateur observations were submitted in UTC, while the professional data were unambiguous in their use of TDB. While it is possible that uncertainties for certain sets of transit data points may have been underestimated, the data come from many amateur and professional sources, and all would have had to make such errors.

Possibly these are transit-timing variations (TTVs) due to interactions with undiscovered planets in the system (Agol et al. 2005), an exploration of which is beyond our present scope. Agol et al. (2005) give a relation for the transit timing deviation for a pair of planets in a mean-motion resonance. An Earth-sized planet in a 2:1 resonance with WASP-43b would produce a maximum timing deviation of 24 seconds. Our typical deviation of 78 seconds suggests a lower limit of 3.2 Earth masses for such a resonance. Other simple-integer ratios of mean motion require larger masses to produce such an effect. WASP-43b's close orbit, and the tidal effects noted above, also raise the possibility that some of the signal may be due to tidal decay. A few calculations will show whether this is likely.

A period change of $\dot{P}$ = -0.65 ± 0.12 s year^{-1} for WASP-43b translates to a change in semi-major axis $\dot{a}$ = (-9.1 ±1.6)×10^{-8} AU year^{-1}. Levrard et al. (2009) give a relation for tidal decay, which for synchronous tidal rotation and negligible eccentricity and obliquity reduces to:

$$\frac{1}{a}\frac{\mathrm{d}a}{\mathrm{d}t} = \frac{6}{Q'_\star}\frac{M_p}{M_\star}\left(\frac{R_\star}{a}\right)^5\left(\omega_\star - \frac{2\pi}{P}\right), \qquad (6)$$

TABLE 5
TRANSIT TIMING DATA.

Mid-Transit Time (BJD_{TDB})	Uncertainty	Source[a]	Quality Rating
2456035.66489	0.0005	George Hall	2
2456015.3273	0.00057	Martin Zíbar	2
2456006.38071	0.00101	Františ̂ek Lomoz	3
2456006.3781	0.00109	Františ̂ek Lomoz	3
2456001.49859	0.00156	Alfonso Carreño	3
2456001.49662	0.00035	Gustavo Muler Schteinman	1
2456001.49531	0.00019	Fernand Emering	1
2455997.43508	0.00086	René Roy	3
2455997.43105	0.00051	Faustino Garcia	3
2455997.43008	0.0004	Nicolas Esseiva	2
2455997.42981	0.00068	Juanjo Gonzalez	3
2455984.41939	0.00064	Ferran Grau Horta	3
2455984.41548	0.00126	Františ̂ek Lomoz	3
2455984.4149	0.00047	Fabio Martinelli	2
2455984.41472	0.00071	Františ̂ek Lomoz	3
2455979.534	0.00044	Nicolas Esseiva	2
2455979.5335	0.0004	Juanjo Gonzalez	2
2455957.57296	0.00122	Františ̂ek Lomoz	4
2455944.55468	0.00106	Roy René	3
2455940.48744	0.0005	Anthony Ayiomamitis	2
2455939.67475	0.00052	Ramon Naves	2
2455933.16473	0.00025	Peter Starr	1
2455686.68399	0.0008	Stan Shadick	3
2455682.61364	0.00039	Tanya Dax, Stacy Irwin	5

[a] The TRansiting ExoplanetS and CAndidates group (TRESCA, http://var2.astro.cz/EN/tresca/index.php) supply their data to the Exoplanet Transit Database (ETD, http://var2.astro.cz/ETD/), which performs the uniform transit analysis described by Poddaný et al. (2010). The ETD web site provided the numbers in this table, which were converted from HJD (UTC) to BJD (TDB).

TABLE 6
ECCENTRIC ORBITAL MODEL.

Parameter	Value
$e\sin\omega$[a]	-0.007 ± 0.010
$e\cos\omega$[a]	-0.0003 ± 0.0006
e	$0.007^{+0.013}_{-0.004}$
ω (°)	-87^{+161}_{-3}
P (days)[a]	$P = 0.81347459 \pm 2.1\times10^{-7}$
T_0 (BJD_{TDB}) [a]	$2{,}455{,}528.86853 \pm 0.00005$
K (m s^{-1})[a]	548 ± 5
γ (m s^{-1})[a]	-3595 ± 4
χ^2	426

[a] Free parameter in MCMC fit

where $Q'_\star$ is the ratio of the stellar tidal quality factor to the second-order stellar tidal Love number, k_2, and $\omega_\star$ is the stellar rotation rate. The quadratic model implies $Q'_\star = 2500 \pm 400$. This is much lower than the values of 10^5 – 10^{10} normally assumed. A small value of $Q'_\star$ was also found by Adams et al. (2010).

Another mechanism to explain orbital decay would be the transfer of orbital angular momentum to another planet in the system instead of to the stellar rotation. If such a planet were in a superior orbit, then it would need a greater orbital angular momentum for divergent planetary migration to occur (Rodriquez et al. 2011).

However, the inferred decay rate (regardless of cause) implies an infall time of order 10^5 years, which is small compared to the estimated age of the star, so neither interpretation is likely. As the curves are quite divergent, fits performed after an additional 1 – 2 observing seasons should resolve the ambiguity.

6. ATMOSPHERE

We modeled the dayside atmosphere of WASP-43b using the atmospheric modeling and retrieval method of Madhusudhan & Seager (2009, 2010). The model computes line-by-line radiative transfer in a one-dimensional, plane-parallel atmosphere, with constraints of local thermodynamic equilibrium, hydrostatic equilibrium, and global energy balance. The pressure-temperature ($P-T$) profile and the molecular composition are free parameters of the model, allowing exploration of models with and without thermal inversions, and those with oxygen-rich as well as carbon-rich compositions (Madhusudhan 2012). The model includes all the primary sources of opacity expected in hydrogen-dominated giant planet atmospheres in the temperature regimes of hot Jupiters, such as WASP-43b. The opacity sources include line-by-line absorption due to H_2O, CO, CH_4, CO_2, and NH_3, and collision-induced absorption (CIA) due to H_2-H_2. We also include hydrocarbons besides CH_4, such as HCN and C_2H_2, which may be abundant in carbon-rich atmospheres (Madhusudhan et al. 2011b; Kopparapu et al. 2012; Madhusudhan 2012). Since in highly irradiated oxygen-rich atmospheres TiO and VO may be abundant (Fortney et al. 2008), we also include line-by-line absorption due to TiO and VO in regions of the atmosphere where the temperatures exceed the corresponding condensation temperatures. Our molecular line data are from Freedman et al. (2008), Freedman (personal communication, 2009), Rothman et al. (2005), Karkoschka & Tomasko (2010), Karkoschka (personal communication, 2011), and Harris et al. (2008). We obtain the H_2-H_2 CIA opacities from Borysow et al. (1997) and Borysow (2002). The volume mixing ratios of all the molecules are free parameters in the model.

We constrain the thermal structure and composition of WASP-43b using our *Spitzer* photometric observations at 3.6 μm and 4.5 μm combined with ground-based photometric data using VLT/HAWK-I at 1.19 μm and 2.1 μm (Gillon et al. 2012). The model also has a joint constraint on the day-night energy redistribution and the Bond albedo, by requiring global energy balance – i.e., that the integrated emergent power from the planet does not exceed the incident irradiation. Given that the number of model parameters is ≥ 10 (depending on the C/O ratio), and the number of available data points is 4, our goal is to find the regions of model space favored by the data, rather than to determine a unique fit. We explore the model parameter space using an MCMC routine (for details, see Madhusudhan & Seager 2009, 2010; Madhusudhan et al. 2011a).

The data rule out a strong thermal inversion in the dayside atmosphere of WASP-43b. The data and two model spectra of atmospheres without thermal inversions are shown in Figure 8. The ground-based and *Spitzer* data provide complementary constraints on the atmospheric properties. The ground-based photometric bandpasses at 1.19 μm and 2.1 μm (Gillon et al. 2012) span spectral regions of low molecular opacity, and, hence, probe the deep layers of the atmosphere at pressures of $P \sim 1$ bar, beyond which the atmosphere is optically thick due to collision-induced opacity. Consequently, the brightness temperatures of the ground-based data constrain the isothermal temperature structure of the deep atmosphere. On the other hand, the two *Spitzer* data sets show lower brightness

TABLE 7
EPHEMERIS SOLUTIONS

Parameter	Linear ephemeris (joint fit)	Linear ephemeris (transits only)	Quadratic ephemeris
T_0 ($\mathrm{BJD_{TDB}}$)	2455528.86853 ± 0.00005	2455581.74441 ± 0.00004	2455581.74433 ± 0.00004
P (days orbit^{-1})	$0.81347459 \pm 2.1\times10^{-7}$	$0.81347395 \pm 2.3\times10^{-7}$	$0.81347788 \pm 7.2\times10^{-7}$
δP (days orbit^{-2})^{a}	0.0	0.0	$(-1.7\pm0.3)\times10^{-8}$
$\dot{P}$ (s yr^{-1})^{b}	0.0	0.0	-0.65 ± 0.12
χ^2		264.3	231.7
BIC		271.4	242.3

[a] $\delta P = \dot{P}P$, [b] Derived parameter

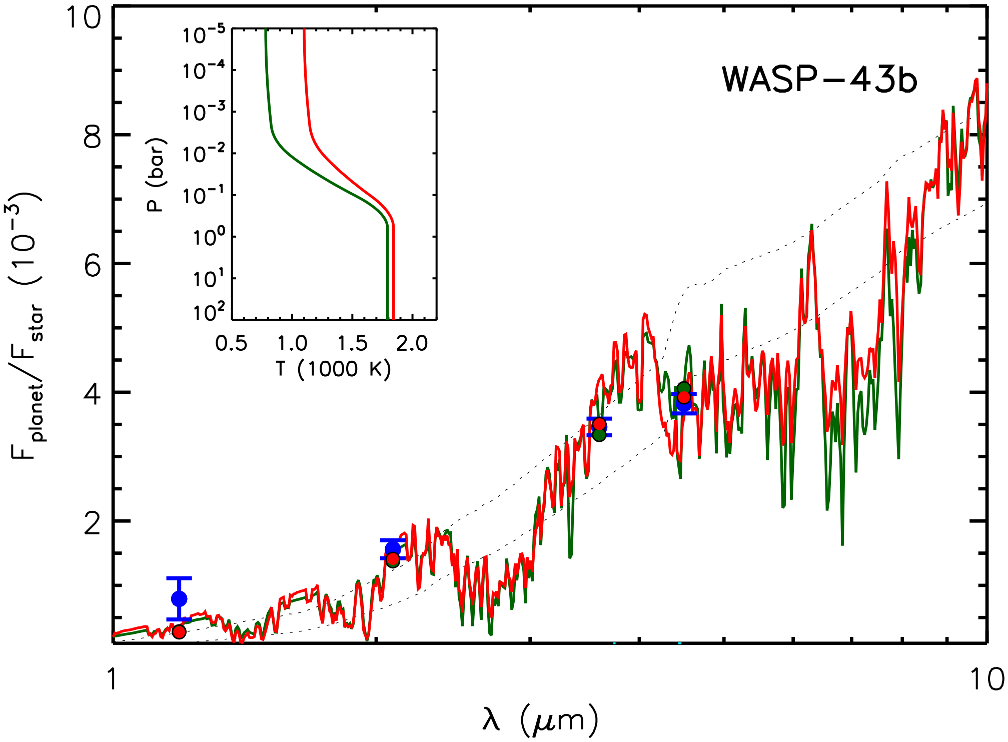

FIG. 8.— Observations and model spectra for dayside thermal emission from WASP-43b. The blue filled circles with error bars show our data in *Spitzer* IRAC channels 1 (3.6 μm) and 2 (4.5 μm) and previously published ground-based data at 1.19 μm and 2.1 μm (Gillon et al. 2012). The solid curves show the model spectra in the main panel, and the corresponding temperature-pressure profiles, with no thermal inversions, in the inset. The green (red) curves correspond to a model with solar (6 × solar) composition. Both models fit the data almost equally well. The dashed curves show blackbody spectra corresponding to planetary brightness temperatures of 1684 K and 1485 K, corresponding to the observed brightness temperatures in the *Spitzer* IRAC channels 1 and 2, respectively.

temperatures at 3.6 μm and 4.5 μm relative to the ground-based data, which is possible only if the temperature structure is decreasing outward in the atmosphere, causing molecular absorption in the *Spitzer* bands. The presence of a strong thermal inversion, on the contrary, would have caused molecular emission leading to higher brightness temperatures in the *Spitzer* bands relative to the ground-based bands. Consequently, the sum total of *Spitzer* and ground-based data rule out a strong thermal inversion in WASP-43b's dayside photosphere.

The molecular composition is less well constrained by the data. Several physically plausible combinations of molecules can explain the absorption in the two *Spitzer* bands (e.g., Madhusudhan & Seager 2010; Madhusudhan 2012). Figure 8 shows two oxygen-rich models in chemical equilibrium, with C/O ratio of 0.5 (solar value), but with different metallicities (solar and six times solar) and thermal profiles, both of which explain the data almost equally well. In both cases, H_2O absorption in the 3.6 μm band, and H_2O, CO, and CO_2 absorption in the 4.5 μm band explain the *Spitzer* data. The fact that the two models fit the data equally well demonstrates the degeneracy between the molecular mixing ratios (via the metallicity) and the temperature gradient. Given the current photometric data, the solar metallicity model with a steep temperature profile (green curve) produces almost as good a fit as the higher metallicity model with a shallower temperature profile (red curve), though the latter fits marginally better. On the other hand, a carbon-rich model with C/O ≥1; (e.g., Madhusudhan 2012), with absorption due to CH_4, CO, C_2H_2, and HCN could also explain the data. However, the current data are insufficient to discriminate between O-rich and C-rich compositions. Thus, new observations are required to obtain more stringent constraints on the chemical composition of WASP-43b. Observations using the *HST* Wide Field Camera 3 in the 1.1 - 1.8 μm bandpass can help constrain the H_2O abundance in the atmosphere. As shown in Figure 8, an O-rich composition predicts strong absorption due to H_2O in the WFC3 bandpass, which would be absent in a carbon-rich atmosphere (Madhusudhan et al. 2011a). Similarly, observations in other molecular bands, such as the CO band at 2.3 μm, can provide constraints on the corresponding molecular mixing ratios.

Our observations provide nominal constraints on the day-night energy redistribution fraction (f_r, Madhusudhan & Seager 2009) in WASP-43b. Our model fits to the combined *Spitzer* and ground-based data allow for up to ∼35% day-night energy redistribution in the planet. However, in the population of models that fit the data, models with higher f_r values require cooler lower atmospheres on the dayside, and hence predict lower fluxes in the ground-based channels. For example, the models shown in Figure 8 have f_r = 32 – 34%, assuming zero Bond albedo. While these models produce an acceptable global fit to all the four data points overall, they predict systematically lower fluxes in the ground-based channels, fitting the ground-based data points only at the σ lower error bars. Considering the ground-based points alone, without the *Spitzer* data, would imply a significantly higher continuum flux, and correspondingly a significantly lower day-night redistribution in the planet than ∼35%, consistent with the finding of Gillon et al. (2012).

The lack of a strong thermal inversion in WASP-43b is not surprising. At an equilibrium temperature of ∼1400 K, the dayside atmosphere of WASP-43b is not expected to host gaseous TiO and VO, which have been proposed to cause thermal inversions (Spiegel et al. 2009; Hubeny et al. 2003; Fortney et al. 2008), though hitherto unknown molecules that could also potentially cause such inversions cannot be ruled out (Zahnle et al. 2009). The lack of a thermal inversion is also consistent with the hypothesis of Knutson et al. (2010), since the host star WASP-43 is known to be active (Hellier et al. 2011).

7. CONCLUSIONS

Exoplanet secondary eclipses provide us with a unique way to observe the dayside spectrum of an irradiated planetary atmosphere, where the opacities of the mixture of atmospheric trace molecules determine the thermal structure of the planetary atmosphere.

WASP-43b has a 0.81 day period, making it one of the shortest-period transiting planets. It has a small semi-major axis (0.01526 ± 0.00018 AU, Gillon et al. 2012). The WASP-43 star is a low mass star ($M_* = 0.717 \pm 0.025$ $M_\odot$, Gillon et al. 2012) and is also one of the coldest of all stars hosting hot Jupiters. The close proximity of the planet probably induces large tidal bulges on the planet's surface (Ragozzine & Wolf 2009). The planet's projected lifetime is also unusually short for such a late-type host star, owing to tidal in-spiral. The estimated lifetime for this planet is of order Myr (Hellier et al. 2011).

In this paper we report two *Spitzer* secondary eclipse observations, using the IRAC 3.6 and 4.5 μm channels. S/N = 26 in channel 1 and 24 in channel 2 allowed non-ambiguous analysis. The final eclipse depths from our joint fit models are 0.346 ± 0.013% and 0.382 ± 0.015%, in channel 1 and 2 respectively. The corresponding brightness temperatures are 1684 ± 24 K and 1485 ± 24 K.

Our secondary eclipse timings, along with the available RV data and transit photometry from the literature and amateur observations, provide better constraints on the orbital parameters. The WASP-43b orbital period is improved by a factor of three ($P = 0.81347459 \pm 2.1\times10^{-7}$ days). We also obtained an upper limit on the eccentricity. The timing of our secondary-eclipse observations is consistent with and suggestive of a circular orbit with $e < 0.0018$.

We combined our *Spitzer* eclipse depths with ground-based data at 1.19 and 2.1 μm from Gillon et al. (2012) to constrain the atmospheric properties of WASP-43b. The data rule out a strong thermal inversion in the dayside atmosphere. This is particularly evident from the fact that our brightness temperatures in both the *Spitzer* channels are lower than those observed in the ground-based channels, suggesting temperatures decreasing outward. Models without thermal inversions and with fiducial oxygen-rich compositions can explain the data. Current data are insufficient to provide stringent constraints on the chemical composition. The data do not suggest very efficient day-night energy redistribution in the planet, consistent with previous studies, though models with up to ∼35% redistribution can explain the data reasonably well.

We thank the observers listed in Table 5 for allowing us to use their results, and the organizers of the Exoplanet Transit Database for coordinating the collection and uniform analysis of these data. We also thank contributors to SciPy, Matplotlib, the Python Programming Language, the free and open-source community, the NASA Astrophysics Data System, and the JPL Solar System Dynamics group for free software and services. The IRAC data are based on observations made with the Spitzer Space Telescope, which is operated by the Jet Propulsion Laboratory, California Institute of Technology, under a contract with NASA. Support for this work was provided by NASA through an award issued by JPL/Caltech; through the Science Mission Directorate's Planetary Atmospheres Program, grant NNX12AI69G; Astrophysics Data Analysis Program, grant NNX13AF38G; and by NASA Headquarters under the NASA Earth and Space Science Fellowship Program, grant NNX12AL83H. NM acknowledges support from the Yale Center for Astronomy and Astrophysics through the YCAA postdoctoral Fellowship.

REFERENCES

Adams, E. R., López-Morales, M., Elliot, J. L., Seager, S., & Osip, D. J. 2010, ApJ, 721, 1829
Agol, E., Steffen, J., Sari, R., & Clarkson, W. 2005, MNRAS, 359, 567
Anderson, D. R., Smith, A. M. S., Lanotte, A. A., Barman, T. S., Campo, C. J., Collier Cameron, A., Gillon, M., Harrington, J., Hellier, C., Maxted, P. F. L., Queloz, D., Triaud, A. H. M. J., & Wheatley, P. J. 2011, A&A, submitted
Arras, P., Burkart, J., Quataert, E., & Weinberg, N. N. 2012, MNRAS, 422, 1761
Batalha, N. M., Rowe, J. F., Bryson, S. T., Barclay, T., Burke, C. J., Caldwell, D. A., Christiansen, J. L., Mullally, F., Thompson, S. E., Brown, T. M., Dupree, A. K., Fabrycky, D. C., Ford, E. B., Fortney, J. J., Gilliland, R. L., Isaacson, H., Latham, D. W., Marcy, G. W., Quinn, S., Ragozzine, D., Shporer, A., Borucki, W. J., Ciardi, D. R., Gautier, III, T. N., Haas, M. R., Jenkins, J. M., Koch, D. G., Lissauer, J. J., Rapin, W., Basri, G. S., Boss, A. P., Buchhave, L. A., Charbonneau, D., Christensen-Dalsgaard, J., Clarke, B. D., Cochran, W. D., Demory, B.-O., Devore, E., Esquerdo, G. A., Everett, M., Fressin, F., Geary, J. C., Girouard, F. R., Gould, A., Hall, J. R., Holman, M. J., Howard, A. W., Howell, S. B., Ibrahim, K. A., Kinemuchi, K., Kjeldsen, H., Klaus, T. C., Li, J., Lucas, P. W., Morris, R. L., Prsa, A., Quintana, E., Sanderfer, D. T., Sasselov, D., Seader, S. E., Smith, J. C., Steffen, J. H., Still, M., Stumpe, M. C., Tarter, J. C., Tenenbaum, P., Torres, G., Twicken, J. D., Uddin, K., Van Cleve, J., Walkowicz, L., & Welsh, W. F. 2012, ArXiv e-prints

Beerer, I. M., Knutson, H. A., Burrows, A., Fortney, J. J., Agol, E., Charbonneau, D., Cowan, N. B., Deming, D., Desert, J.-M., Langton, J., Laughlin, G., Lewis, N. K., & Showman, A. P. 2011, ApJ, 727, 23

Berta, Z. K., Charbonneau, D., Désert, J.-M., Miller-Ricci Kempton, E., McCullough, P. R., Burke, C. J., Fortney, J. J., Irwin, J., Nutzman, P., & Homeier, D. 2012, ApJ, 747, 35

Blecic, J., Harrington, J., Madhusudhan, N., Stevenson, K. B., Hardy, R., Cubillos, P., Hardin, M., Campo, C., Bowman, W. C., Nymeyer, S., Anderson, D. R., Maxted, P. F. L., & Loredo, T. J. 2013, ApJ, submitted, arXiv:1111.2363

Borucki, W. J., Koch, D. G., Basri, G., Batalha, N., Brown, T. M., Bryson, S. T., Caldwell, D., Christensen-Dalsgaard, J., Cochran, W. D., DeVore, E., Dunham, E. W., Gautier, III, T. N., Geary, J. C., Gilliland, R., Gould, A., Howell, S. B., Jenkins, J. M., Latham, D. W., Lissauer, J. J., Marcy, G. W., Rowe, J., Sasselov, D., Boss, A., Charbonneau, D., Ciardi, D., Doyle, L., Dupree, A. K., Ford, E. B., Fortney, J., Holman, M. J., Seager, S., Steffen, J. H., Tarter, J., Welsh, W. F., Allen, C., Buchhave, L. A., Christiansen, J. L., Clarke, B. D., Das, S., Désert, J.-M., Endl, M., Fabrycky, D., Fressin, F., Haas, M., Horch, E., Howard, A., Isaacson, H., Kjeldsen, H., Kolodziejczak, J., Kulesa, C., Li, J., Lucas, P. W., Machalek, P., McCarthy, D., MacQueen, P., Meibom, S., Miquel, T., Prsa, A., Quinn, S. N., Quintana, E. V., Ragozzine, D., Sherry, W., Shporer, A., Tenenbaum, P., Torres, G., Twicken, J. D., Van Cleve, J., Walkowicz, L., Witteborn, F. C., & Still, M. 2011, ApJ, 736, 19

Borysow, A. 2002, A&A, 390, 779

Borysow, A., Jorgensen, U. G., & Zheng, C. 1997, A&A, 324, 185

Campo, C. J., Harrington, J., Hardy, R. A., Stevenson, K. B., Nymeyer, S., Ragozzine, D., Lust, N. B., Anderson, D. R., Collier-Cameron, A., Blecic, J., Britt, C. B. T., Bowman, W. C., Wheatley, P. J., Loredo, T. J., Deming, D., Hebb, L., Hellier, C., Maxted, P. F. L., Pollaco, D., & West, R. G. 2011, ApJ, 727, 125

Charbonneau, D., Allen, L. E., Megeath, S. T., Torres, G., Alonso, R., Brown, T. M., Gilliland, R. L., Latham, D. W., Mandushev, G., O'Donovan, F. T., & Sozzetti, A. 2005, ApJ, 626, 523

Cowan, N. B., Machalek, P., Croll, B., Shekhtman, L. M., Burrows, A., Deming, D., Greene, T., & Hora, J. L. 2012a, ApJ, 747, 82

Cowan, N. B., Voigt, A., & Abbot, D. S. 2012b, ApJ, 757, 80

Crossfield, I. J. M., Barman, T., Hansen, B. M. S., Tanaka, I., & Kodama, T. 2012, ApJ, 760, 140

Crossfield, I. J. M., Hansen, B. M. S., Harrington, J., Cho, J., Deming, D., Menou, K., & Seager, S. 2010, ApJ, 723, 1436

Cubillos, P., Harrington, J., N, M., Stevenson, K., Hardy, R., Blecic, J., D, A., M, H., & Campo, C. 2013, ApJ, Submitted

de Wit, J., Gillon, M., Demory, B.-O., & Seager, S. 2012, A&A, 548, A128

Deming, D., Knutson, H., Agol, E., Desert, J.-M., Burrows, A., Fortney, J. J., Charbonneau, D., Cowan, N. B., Laughlin, G., Langton, J., Showman, A. P., & Lewis, N. K. 2011, ApJ, 726, 95

Deming, D., Wilkins, A., McCullough, P., Burrows, A., Fortney, J. J., Agol, E., Dobbs-Dixon, I., Madhusudhan, N., Crouzet, N., Desert, J.-M., Gilliland, R. L., Haynes, K., Knutson, H. A., Line, M., Magic, Z., Mandell, A. M., Ranjan, S., Charbonneau, D., Clampin, M., Seager, S., & Showman, A. P. 2013, ArXiv e-prints

Demory, B.-O., Gillon, M., Barman, T., Bonfils, X., Mayor, M., Mazeh, T., Queloz, D., Udry, S., Bouchy, F., Delfosse, X., Forveille, T., Mallmann, F., Pepe, F., & Perrier, C. 2007, A&A, 475, 1125

Desert, J.-M., Charbonneau, D., Fressin, F., & Torres, G. 2012, in American Astronomical Society Meeting Abstracts, Vol. 219, American Astronomical Society Meeting Abstracts, 414.02

Eastman, J., Siverd, R., & Gaudi, B. S. 2010, PASP, 122, 935

Fazio, G. G. et al. 2004, Astrophy. J. Suppl. Ser., 154, 10

Fortney, J. J., Lodders, K., Marley, M. S., & Freedman, R. S. 2008, ApJ, 678, 1419

Fortney, J. J., Marley, M. S., Hubickyj, O., Bodenheimer, P., & Lissauer, J. J. 2005, Astronomische Nachrichten, 326, 925

Fraine, J. D., Deming, D., Gillon, M., Jehin, E., Demory, B.-O., Benneke, B., Seager, S., Lewis, N. K., Knutson, H., & Desert, J.-M. 2013, ArXiv e-prints

Freedman, R. S., Marley, M. S., & Lodders, K. 2008, ApJS, 174, 504

Gelman, A. 2002, Encyclopedia of Environmetrics, 3, 1634âĂŞ1637

Gelman, A. & Rubin, D. 1992, Statistical Science, 7, 457

Gibson, N. P., Aigrain, S., Pont, F., Sing, D. K., Désert, J.-M., Evans, T. M., Henry, G., Husnoo, N., & Knutson, H. 2012, MNRAS, 422, 753

Gillon, M., Triaud, A. H. M. J., Fortney, J. J., Demory, B.-O., Jehin, E., Lendl, M., Magain, P., Kabath, P., Queloz, D., Alonso, R., Anderson, D. R., Collier Cameron, A., Fumel, A., Hebb, L., Hellier, C., Lanotte, A., Maxted, P. F. L., Mowlavi, N., & Smalley, B. 2012, A&A, 542, A4

Harrington, J., Luszcz, S., Seager, S., Deming, D., & Richardson, L. J. 2007, Nature, 447, 691

Harris, G. J., Larner, F. C., Tennyson, J., Kaminsky, B. M., Pavlenko, Y. V., & Jones, H. R. A. 2008, MNRAS, 390, 143

Hellier, C., Anderson, D. R., Collier Cameron, A., Gillon, M., Jehin, E., Lendl, M., Maxted, P. F. L., Pepe, F., Pollacco, D., Queloz, D., Ségransan, D., Smalley, B., Smith, A. M. S., Southworth, J., Triaud, A. H. M. J., Udry, S., & West, R. G. 2011, A&A, 535, L7

Hubeny, I., Burrows, A., & Sudarsky, D. 2003, ApJ, 594, 1011

Karkoschka, E. & Tomasko, M. G. 2010, Icarus, 205, 674

Knutson, H. A., Charbonneau, D., Cowan, N. B., Fortney, J. J., Showman, A. P., Agol, E., & Henry, G. W. 2009, ApJ, 703, 769

Knutson, H. A., Howard, A. W., & Isaacson, H. 2010, ApJ, 720, 1569

Knutson, H. A., Lewis, N., Fortney, J. J., Burrows, A., Showman, A. P., Cowan, N. B., Agol, E., Aigrain, S., Charbonneau, D., Deming, D., Désert, J.-M., Henry, G. W., Langton, J., & Laughlin, G. 2012, ApJ, 754, 22

Knutson, H. A., Madhusudhan, N., Cowan, N. B., Christiansen, J. L., Agol, E., Deming, D., Désert, J.-M., Charbonneau, D., Henry, G. W., Homeier, D., Langton, J., Laughlin, G., & Seager, S. 2011, ApJ, 735, 27

Kopparapu, R. k., Kasting, J. F., & Zahnle, K. J. 2012, ApJ, 745, 77

Levrard, B., Winisdoerffer, C., & Chabrier, G. 2009, ApJ, 692, L9

Lewis, N. K., Knutson, H. A., Showman, A. P., Cowan, N. B., Laughlin, G., Burrows, A., Deming, D., Crepp, J. R., Mighell, K. J., Agol, E., Bakos, G. Á., Charbonneau, D., Désert, J.-M., Fischer, D. A., Fortney, J. J., Hartman, J. D., Hinkley, S., Howard, A. W., Johnson, J. A., Kao, M., Langton, J., Marcy, G. W., & Winn, J. N. 2013, ArXiv e-prints

López-Morales, M., Coughlin, J. L., Sing, D. K., Burrows, A., Apai, D., Rogers, J. C., Spiegel, D. S., & Adams, E. R. 2010, ApJ, 716, L36

Madhusudhan, N. 2012, ArXiv e-prints

Madhusudhan, N., Harrington, J., Stevenson, K. B., Nymeyer, S., Campo, C. J., Wheatley, P. J., Deming, D., Blecic, J., Hardy, R. A., Lust, N. B., Anderson, D. R., Collier-Cameron, A., Britt, C. B. T., Bowman, W. C., Hebb, L., Hellier, C., Maxted, P. F. L., Pollacco, D., & West, R. G. 2011a, Nature, 469, 64

Madhusudhan, N., Mousis, O., Johnson, T. V., & Lunine, J. I. 2011b, ApJ, 743, 191

Madhusudhan, N. & Seager, S. 2009, ApJ, 707, 24

—. 2010, ApJ, 725, 261

Majeau, C., Agol, E., & Cowan, N. B. 2012, ApJ, 747, L20

Mandel, K. & Agol, E. 2002, ApJ, 580, L171

Nymeyer, S., Harrington, J., Campo, C., Hardy, R., Stevenson, K. B., Lust, N. B., Collier Cameron, A., Loredo, T. J., Blecic, J., Britt, C. B. T., Bowman, W. C., Wheatley, P. J., Deming, D., Hebb, L., Hellier, C., Maxted, P. F. L., Pollacco, D., & West, R. G. 2011, ApJ, 742, 35

Poddaný, S., Brát, L., & Pejcha, O. 2010, ArXiv Astrophysics e-prints, 15, 297

Pont, F., Zucker, S., & Queloz, D. 2006, MNRAS, 373, 231

Ragozzine, D. & Wolf, A. S. 2009, ApJ, 698, 1778

Reach, W. T., Megeath, S. T., Cohen, M., Hora, J., Carey, S., Surace, J., Willner, S. P., Barmby, P., Wilson, G., Glaccum, W., Lowrance, P., Marengo, M., & Fazio, G. G. 2005, PASP, 117, 978

Rodriquez, A., Michtchenko, T. A., & Miloni, O. 2011, Celestial Mechanics and Dynamical Astronomy, 111, 161

Rothman, L. S., Jacquemart, D., Barbe, A., Chris Benner, D., Birk, M., Brown, L. R., Carleer, M. R., Chackerian, C., Chance, K., Coudert, L. H., Dana, V., Devi, V. M., Flaud, J.-M., Gamache, R. R., Goldman, A., Hartmann, J.-M., Jucks, K. W., Maki, A. G., Mandin, J.-Y., Massie, S. T., Orphal, J., Perrin, A., Rinsland, C. P., Smith, M. A. H., Tennyson, J., Tolchenov, R. N., Toth, R. A., Vander Auwera, J., Varanasi, P., & Wagner, G. 2005, J. Quant. Spec. Radiat. Transf., 96, 139

Showman, A. P., Fortney, J. J., Lian, Y., Marley, M. S., Freedman, R. S., Knutson, H. A., & Charbonneau, D. 2009, ApJ, 699, 564

Showman, A. P. & Guillot, T. 2002, A&A, 385, 166

Spiegel, D. S., Silverio, K., & Burrows, A. 2009, ApJ, 699, 1487

Stevenson, K. B., Harrington, J., Fortney, J. J., Loredo, T. J., Hardy, R. A., Nymeyer, S., Bowman, W. C., Cubillos, P., Bowman, M. O., & Hardin, M. 2012, ApJ, 754, 136

Stevenson, K. B., Harrington, J., Nymeyer, S., Madhusudhan, N., Seager, S., Bowman, W. C., Hardy, R. A., Deming, D., Rauscher, E., & Lust, N. B. 2010, Nature, 464, 1161

Todorov, K. O., Deming, D., Knutson, H. A., Burrows, A., Sada, P. V., Cowan, N. B., Agol, E., Desert, J.-M., Fortney, J. J., Charbonneau, D., Laughlin, G., Langton, J., Showman, A. P., & Lewis, N. K. 2012, ApJ, 746, 111

Winn, J. N., Holman, M. J., Torres, G., McCullough, P., Johns-Krull, C., Latham, D. W., Shporer, A., Mazeh, T., Garcia-Melendo, E., Foote, C., Esquerdo, G., & Everett, M. 2008, ApJ, 683, 1076

Zahnle, K., Marley, M. S., & Fortney, J. J. 2009, ApJ, submitted

A. SYSTEM PARAMETERS

TABLE 8
SYSTEM PARAMETERS OF WASP-43.

PARAMETER	VALUE	REFERENCE
Eclipse Parameters		
Eclipse Midpoint ($\mathrm{BJD_{TDB}}$) (2011-07-30)	2455773.3179 ± 0.0003	a
Eclipse Midpoint ($\mathrm{BJD_{TDB}}$) (2011-07-29)	2455772.5045 ± 0.0003	a
Eclipse Duration t_{4-1} (hrs)	1.25 ± 0.02	a
Eclipse Depth *Spitzer* IRAC, 3.6 μm (%)	0.346 ± 0.013	a
Eclipse Depth *Spitzer* IRAC, 4.5 μm (%)	0.382 ± 0.015	a
Eclipse Depth *VLT* HAWK-I, 2.095 μm (ppm)	1560 ± 140	c
Eclipse Depth *VLT* HAWK-I, 1.186 μm (ppm)	790 ± 320	c
Ingress/Egress Time t_{2-1} (hrs)	0.264 ± 0.018	a
Orbital Parameters		
Orbital Period, P (days)	$0.81347459 \pm 2.1\times10^{-7}$	b
Semimajor axis, a (AU)	0.01526 ± 0.00018	c
Transit Time ($\mathrm{BJD_{TDB}}$)	2455726.54336 ± 0.00012	c
Orbital eccentricity, e	$0.007^{+0.013}_{-0.004}$	b
Argument of pericenter, ω (deg)	-87^{+161}_{-3}	b
Velocity semiamplitude, K ($\mathrm{m\,s^{-1}}$)	548 ± 5	b
Center-of-mass velocity γ ($\mathrm{m\,s^{-1}}$)	-3595 ± 4	b
Stellar Parameters		
Spectral Type	KV7	c
Mass, M_* ($M_\odot$)	0.717 ± 0.025	c
Radius, R_* ($R_\odot$)	$0.667^{+0.011}_{-0.010}$	c
Mean density, ρ_* ($\rho_\odot$)	$2.410^{+0.079}_{-0.075}$	c
Effective temperature, T_{eff} (K)	4520 ± 120	c
Surface gravity, log g_* (cgs)	$4.645^{+0.011}_{-0.010}$	c
Projected rotation rate, $v_* \sin(i)$ ($\mathrm{kms^{-1}}$)	4.0 ± 0.4	c
Metallicity [Fe/H] (dex)	-0.01 ± 0.12	c
Distance (pc)	80 ± 20	d
Planetary Parameters		
Mass, M_{p} (M_{J})	$2.034^{+0.052}_{-0.051}$	c
Radius, R_{p} (R_{J})	1.036 ± 0.019	c
Surface gravity, log g_{p} (cgs)	$3.672^{+0.013}_{-0.012}$	c
Mean density, ρ_{p} ($\mathrm{g\,cm^{-3}}$)	$1.377^{+0.063}_{-0.059}$	c
Equilibrium temperature (A=0), T_{eq} (K)	1440^{+40}_{-39}	c

a - this work (parameters derived using 2-joint fit, see Section 4.3)
b - this work (see Section 5)
c - Gillon et al. (2012)
d - Hellier et al. (2011)